Journal of
Nanoscience and Nanotechnology
Vol. 10, 3145–3154, 2010

RESEARCH ARTICLE

On the Application of Different Bimetallic Alloy Nanoparticle Combinations in Fiber Optic Surface Plasmon Resonance Salinity Sensor and Its Performance Optimization Against Thermal Effects

Anuj K. Sharma* and Gerhard J. Mohr

Institute of Physical Chemistry, Friedrich Schiller University, Lessingstrasse 10, 07743 Jena, Germany

In the present work, we have theoretically investigated the capability of the layer composed of various combinations of bimetallic alloy nanoparticles to be used in fiber optic salinity sensor based on the technique of surface plasmon resonance (SPR). The metals considered for the present analysis are silver, gold, copper, and aluminum. The performance of the sensor with six different bimetallic alloy nanoparticle combinations is evaluated and compared. Furthermore, the performance optimization is carried out in order to minimize the effect of the variation in operating temperature. The overall performance is analyzed in terms of four parameters: sensitivity, signal-to-noise ratio, detection limit, and operating range for the salinity detection in the water sample. On the basis of the comparisons and logistic criteria, the best possible bimetallic alloy combinations along with requisite alloy composition ratio are predicted. The nanoparticle layer made of bimetallic alloy is capable of simultaneously providing larger values of sensitivity, signal-to-noise ratio, detection and operating range, against the temperature-variation compared to single metallic nanoparticle layer.

Keywords: Surface Plasmon Resonance, Optical Fiber, Bimetallic Alloy Nanoparticle, Salinity Sensor, Thermo-Optic Effect.

1. INTRODUCTION

In the last two decades, the optical phenomenon of surface plasmon resonance (SPR) has become an important analytical tool for fast and precise detection of several physical, chemical, and bio-chemical parameters.[1–4] In the SPR technique, a metal-dielectric interface supports a p-polarized electromagnetic wave, i.e., the surface plasmon wave (SPW), propagating along the interface. In Kretschmann's attenuated total reflection (ATR) configuration,[5] when the p-polarized light with propagation constant (and energy) matching to that of the SPW is incident on such metal-dielectric interface, an evanescent wave is generated. The coupling of the evanescent wave and SPW gives rise to a strong absorption of incident light and the output signal demonstrates a sharp dip at a particular wavelength known as resonance wavelength. The resonance condition is given by following expression

$$K_0 n_c \sin\theta = \mathrm{Re}\left[K_0\left(\frac{\varepsilon_m \varepsilon_s}{\varepsilon_m + \varepsilon_s}\right)^{1/2}\right]; \quad K_0 = \frac{2\pi}{\lambda} \quad (1)$$

The term on the left is the propagation constant (K_{ev}) of the evanescent wave corresponding to the light incident at an angle θ through a light coupling device (such as prism or optical fiber) of refractive index n_c. The term on the right is the real part of SPW propagation constant (K_{SP}) with ε_m as metal dielectric constant and ε_s as the dielectric constant of sensing (dielectric) medium. This matching condition of propagation constants is strongly sensitive to even a slight change in the outer ambience, which makes SPR technique a powerful tool for sensing of different parameters. In general, SPR is excited at the surface of a thin metal layer attached to a light-coupling device according to Kretschmann's ATR method. Although the use of thin layer is still very popular among the researchers for sensing purposes, the focus of research has recently shifted more towards metal nanoparticles in SPR sensing applications. Biosensors and chemical sensors based on metal

*Author to whom correspondence should be addressed.

1533-4880/2010/10/3145/0010 doi:10.1166/jnn.2010.2391

nanoparticles have been proposed with enhanced sensitivity, and faster response.[6–9]

The above resonance condition for plasmon excitation remains the same for metal nanoparticles. However, in case of nanoparticles, the metal dielectric constant (ε_m) is now dependent on size, shape, and their total distribution, causing a significant difference in SPR sensor's performance. It has been shown in a previous study that fiber optic SPR sensors with bimetallic alloy nanoparticles exhibit better performance than those with other distribution of metal nanoparticles such as core–shell one.[7] Furthermore, the fiber optic SPR sensors with different bimetallic alloy nanoparticles are able to show a balanced sensing performance because of their varying optical properties, which can efficiently reduce the usual trade-off between sensitivity and accuracy of an SPR sensor.[9] In addition, there are some other external factors that may affect the performance of the SPR sensor and temperature being the most prominent because the thermo-optic effect (among the metals and dielectric media) causes a significant change in the resonance condition. Any variation or fluctuation in the operating temperature affects the SPR sensor's sensitivity and detection accuracy due to variation in resonance condition. For instance, if a fiber optic SPR sensor is to be used for the quantification of salinity in water samples, then it is very critical to optimize the sensor's performance not only with respect to salinity but also to temperature variation. Salinity is a measure of the salt concentration in water and is estimated by the amount of sodium chloride (in grams) present in water (in Kg). Naturally, the monitoring of salinity may have to be carried out at different temperatures.

In the present work, we propose a SPR-based fiber optic salinity sensor with different bimetallic alloy nanoparticles made out of four metals: Ag, Au, Al, and Cu. The analysis is carried out separately for all six bimetallic alloy combinations and a comparison in terms of their sensitivity and signal-to-noise ratio (SNR) is carried out to predict the conditions for the best sensing performance. Furthermore, the influence of temperature on the sensor's performance is analyzed by taking into account the thermo-optic effect in all the concerned layers. The sensor's performance is then optimized against the temperature-variation. The wavelength interrogation method in combination with optical fiber is used for the analysis. Finally, the most suitable bimetallic alloy combinations with their optimized range of alloy fractions are predicted in order to provide an optimized salinity detection at fixed as well as varying temperatures.

2. THEORETICAL MODEL

The attenuated total reflection (ATR) method along with the Kretschmann configuration is generally used in SPR measurements. In the fiber optic SPR sensor, the cladding around the core of a multimode step-index optical fiber is removed and is coated with a bimetallic nanoparticle alloy layer of thickness d. This bimetallic nanoparticle layer is finally covered with the sensing layer (Fig. 1). The light from a polychromatic source is launched into one of the ends of the fiber and is detected at the other end. We now discuss the main thermal and spectral properties of all the constituents of the sensor.

2.1. Fiber Core

For the present analysis, the central core of optical fiber is assumed to be made of fused silica. The dielectric constant of silica varies with wavelength of light source as well as temperature of the environment due to material dispersion and thermo-optic effect, respectively. If T_f is the operating temperature, the wavelength (λ) and temperature dependent dielectric constant of silica may be efficiently represented by the following empirical expression[10]

$$\varepsilon_{\text{silica}}(\lambda, T_f) = 1.31552 + A_1 T_f + \frac{(A_2 + A_3 T_f)\lambda^2}{\lambda^2 - (A_4 + A_5 T_f)} + \frac{(A_6 + A_7 T_f)\lambda^2}{\lambda^2 - 100} \quad (2)$$

The numeric values of the coefficients from A_1 to A_7 have been given in Table I.

2.2. Bimetallic Alloy Nanoparticle Layer

According to Drude formula, the dielectric function (ε_m) of any metal can be written as:

$$\varepsilon_m(\lambda) = \varepsilon_{mr} + i\varepsilon_{mi} = 1 - \frac{\lambda^2}{\lambda_p^2(1 + i(\lambda/\lambda_c))} \quad (3)$$

where λ_p and λ_c denote the plasma wavelength and the collision wavelength, respectively. These are given by:

$$\frac{1}{\lambda_p} = \sqrt{\frac{Ne^2}{4\pi^2 c^2 m \varepsilon_0}} \quad (4)$$

and,

$$\frac{1}{\lambda_c} = \frac{v_f}{2\pi c R_{\text{bulk}}} \quad (5)$$

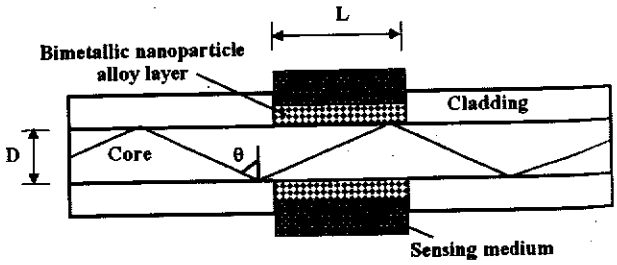

Fig. 1. A fiber optic SPR sensor with bimetallic nanoparticle alloy layers.

Table I. Parameters used for the calculation of dielectric constant of silica.

Parameter	Numeric value
A_1	6.90754×10^{-6}
A_2	0.788404
A_3	2.35835×10^{-5}
A_4	0.0110199
A_5	5.84758×10^{-7}
A_6	0.91316
A_7	5.48368×10^{-7}

where N represents the concentration of free electrons; m and e represent the effective mass and the charge of the electron, respectively; ε_0 is the permittivity of the vacuum; c is the velocity of light. R_{bulk} represents the mean free path of the conduction electrons, and v_f represents the velocity of the electrons at the Fermi energy.

2.2.1. Size Dependence: Surface Scattering

When the particle radius, R_{particle}, is smaller than the mean free path in the bulk metal, conduction electrons are additionally scattered by the surface, and the effective mean free path, R_{eff}, becomes size dependent with

$$\frac{1}{R_{\text{eff}}} = \frac{1}{R_{\text{bulk}}} + \frac{1}{R_{\text{particle}}} \tag{6}$$

Hence, the size dependence of the collision (or damping) wavelength is given by

$$\frac{1}{\lambda_c(R_{\text{particle}})} = \frac{1}{\lambda_c(\text{bulk})} + \frac{v_f}{2\pi c R_{\text{particle}}} \tag{7}$$

Equation (5) has been experimentally verified for spherical metal nanoparticles right down to a size of 2 nm.[11] Thus, Eq. (3) together with (4) to (7) completely represents the size dependent dielectric function of a metal nanoparticle even down to a size of 2 nm.

2.2.2. Temperature Dependence: Phonon–Electron and Electron–Electron Scattering

The origin of the temperature dependence of the plasma wavelength (λ_p) is the temperature dependences of the density and the effective mass of electrons. If T_f is the operating temperature, the temperature dependent plasma oscillation wavelength is given by[12]

$$\frac{1}{\lambda_p(T_f)} = \frac{1}{\lambda_{p0}}[1 + 3\gamma_m(T_f - T_0)]^{-1/2} \tag{8}$$

where γ_m is the thermal linear expansion coefficient of the metal and T_0 is the room temperature which acts as the reference temperature. λ_{p0} is the plasma frequency of the metal at room temperature.

The temperature dependence of collision wavelength of metal nanoparticles is due to two factors: phonon–electron scattering, and electron–electron scattering. Their contributions are λ_{cp}, and λ_{ce}, respectively. The combined effect of the two factors, with taking particle size dependence into account, is represented as:

$$\frac{1}{\lambda_c(T_f, R_{\text{particle}})} = \frac{1}{\lambda_{cp}(T_f)} + \frac{1}{\lambda_{ce}(T_f)} + \frac{v_f}{2\pi c R_{\text{particle}}} \tag{9}$$

The separation of the above three terms gives an indication that all these three different phenomena are independent from one another. For instance, if the nanoparticle size is very large, then the third term has no effect on collision wavelength and this phenomenon occurs irrespective of the variation in operating temperature. Moreover, in most of the SPR thermal models,[12, 13] phonon–electron scattering and electron–electron scattering are considered to be independent from each other.

Now, λ_{cp} can be modeled by using the Holstein model of phonon–electron scattering.[14] The derivation is based on the simple Debye model for the phonon spectrum and is valid assuming $E_F \gg k_B T_f, k_B T_D$, where E_F is the Fermi energy, k_B is the Boltzmann constant, and T_D is the Debye temperature. In its final form, Holstein expression, in terms of plasma wavelength, becomes:[15, 16]

$$\frac{1}{\lambda_{cp}(T_f)} = \frac{2\pi c \varepsilon_0}{\lambda_p^2 \sigma(0)} \frac{\left[1/10 + (T_f/T_D)^5 \int_0^{T_D/T} z^4/(e^z - 1)dz\right]}{\int_0^1 (z^5/(e^z - 1)(1 - e^{-z}))\, dz} \tag{10}$$

In Eq. (10), $\sigma(0)$ is the dc-conductivity and ε_0 is the permittivity of the vacuum.

Next is the electron–electron scattering wavelength (λ_{ce}), which is evaluated by the model, proposed by Lawrence.[17] The corresponding result can be obtained in terms of the Fermi energy E_F of the metal electrons as follows:

$$\frac{1}{\lambda_{ce}(T_f)} = \frac{\pi^3 \Gamma \Delta}{12 c h E_F}\left[(k_B T_f)^2 + \left(\frac{h\omega}{4\pi^2}\right)^2\right] \tag{11}$$

In Eq. (11), h is the Planck constant; Γ is a constant giving the average over the Fermi surface of the scattering probability and Δ represents the fractional unklapp scattering. Thus, Eq. (3) together with Eqs. (8) to (11) efficiently represents the temperature-dependence of the dielectric constant of the metal nanoparticle. The values of the constants and parameters for different metal nanoparticle layer used for numerical simulations are given in Table II.[12–18] The average dielectric constant (ε_A) of bimetallic alloy could be assumed to vary with the composition-weighted average of the dielectric constants (say, ε_{m1} and ε_{m2}) of two metals and is given by[9]

$$\varepsilon_A(x, \lambda, T_f) = x\varepsilon_{m1}(\lambda, T_f) + (1 - x)\varepsilon_{m2}(\lambda, T_f) \tag{12}$$

where x is the volume fraction (or alloy fraction, or composition ratio) of the nanoparticles of first metal.

Table II. Metal parameters used for the numerical simulation.

Parameter	Ag	Au	Al	Cu
λ_{p0} (in m)	1.4541×10^{-7}	1.6826×10^{-7}	1.0657×10^{-7}	1.3617×10^{-7}
γ_m (in K^{-1})	1.89×10^{-5}	1.42×10^{-5}	2.40×10^{-5}	1.48×10^{-5}
T_D (in K)	215	170	396	320
E_F (in eV)	5.48	5.53	11.7	7.0
$1/\sigma(0)$ (in Ωcm)	1.16×10^{-6}	1.32×10^{-6}	3.90×10^{-6}	1.85×10^{-6}
Δ	0.73	0.77	0.75	0.79
Γ	0.55	0.55	0.52	0.57
v_f (m/s)	1.40×10^{6}	1.40×10^{6}	2.02×10^{6}	1.57×10^{6}

2.3. Sensing Layer

In order to evaluate the effect of temperature on sensor's sensitivity and SNR, we must consider two different samples with slightly different refractive indices. For the present study, we have considered pure and saline water (i.e., pure water having a small amount of salinity) as two samples. The refractive indices of both these samples vary with temperature, density and wavelength. We used the following Lorentz-Lorentz relation for the refractive index (n_s) of pure water[19]

$$\left(\frac{n_s^2-1}{n_s^2-1}\right)\frac{1}{\rho^*} = a_0 + a_1\rho^* + a_2T_f^* + a_3\lambda^{*2}T_f^* + \frac{a_4}{\lambda^{*2}} + \frac{a_5}{\lambda^{*2}-\lambda_{UV}^2} + \frac{a_6}{\lambda^{*2}-\lambda_{IR}^2} + a_7\rho^{*2} \tag{13}$$

where $\rho^* = \rho/\rho_0$; $\rho_0 = 1000$ kg/m^3, $\lambda^* = \lambda/\lambda_0$; $\lambda_0 = 0.589$ μm, $T_f^* = T_f/T_0$; $T_0 = 273.15$ K.

In above equation, ρ is the density (in kg/m^3), λ is the wavelength of the light (in μm), and T_f is the operating temperature (in K). Now, we describe how the above equation holds differently for pure water and saline water.

In Eq. (13), density (ρ) of water is also temperature dependent. The density of water further changes depending on the amount of salt it contains. The temperature-dependent variation of density of pure water (i.e., no salt) is represented according to following empirical formula:[20]

Pure water:

$$\rho(T) = \frac{1000(1-T-288.9414)}{508929.2(T+68.12963)(T-3.9863)^2} \tag{14}$$

When the water contains some amount of salt, the density becomes dependent on temperature as well as salinity of the water sample. The dependence of density on temperature and salinity (S) is represented according to following empirical formula:[20]

Saline water:

$$\rho(T) = \rho_0 + A(T)S + B(T)S^{3/2} + CS^2 \tag{15}$$

with

$$A(T) = 0.824493 - (4.0899\times10^{-3})T + (7.6438\times10^{-5})T^2 + (8.2467\times10^{-7})T^3 + (5.3675\times10^{-9})T^4$$

$$B(T) = -(5.724\times10^{-3}) + (1.0227\times10^{-4})T + (1.6546\times10^{-6})T^2$$

$$C = 4.8314\times10^{-4}$$

In Eqs. (14) and (15), temperature ($T = T_f - T_0$) is given in °C. In Eq. (15), salinity (S) is given in g/Kg. It is worth-mentioning that the above empirical relations for sensing layer (i.e., Eqs. (13–15)) as well as that for fiber core (i.e., Eq. (2)), used in the present scheme are experimentally verified. Therefore, application of these relations makes it possible to analyze the present model under as closer practical conditions as possible.

2.4. Performance Parameters

To obtain the expression for intensity reflection coefficient (R_p) for the p-polarized incident beam we have used the matrix method for a multilayer system.[7] Furthermore, the normalized transmitted power (P_{trans}) at the output end of the fiber is calculated for all-guided rays launching as we carried out in our previous study for fiber optic SPR sensor based on Ag–Au bimetallic alloy nanoparticle layers.[7]

There are mainly two important performance parameters of SPR sensor. These are sensitivity and signal to noise ratio (SNR). The sensitivity and SNR should be as high as possible for a sensor. In the SPR sensor based on wavelength interrogation, as discussed earlier, the resonance wavelength (λ_{res}) is determined corresponding to the parameter to be measured. Suppose, if a small amount of salt is added to pure water (of refractive index n_s), and the refractive index of the water sample (sensing medium) is altered by δn_s, then the resonance wavelength also shifts from λ_{res} to $\lambda_{res}+\delta\lambda_{res}$ (Fig. 2). The sensitivity (S_n) of the sensor is defined as[4]

$$S_n = \frac{\delta\lambda_{res}}{\delta n_s} \tag{16}$$

In the present case, the above definition of sensitivity is required because apart from salinity, the refractive index of the water sample depends on wavelength as well as operating temperature. Therefore, the above sensitivity definition enables an accomplished evaluation of the sensor's performance.

The accuracy of the detection of SPR wavelength (λ_{res}) further depends on the width of the response curve. The spectral width of the SPR curve should be small for an accurate measurement of the resonance wavelength. Therefore, if $\delta\lambda_{SW}$ is the mean spectral width of the SPR curves corresponding to two sensing media at some reference output power value, the SNR of the SPR sensor utilizing spectral interrogation can be written as (Fig. 2)[7]

$$\text{SNR} = \frac{\delta\lambda_{res}}{\delta\lambda_{SW}} \tag{17}$$

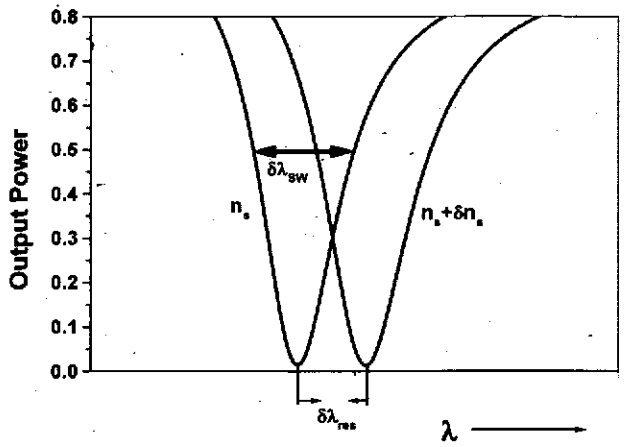

Fig. 2. The shift in resonance wavelength ($\delta\lambda_{res}$) with a change in refractive index of the sensing layer (n_s) by δn_s. $\delta\lambda_{SW}$ is the spectral width of the curve at any reference value of output power corresponding to sensing layer refractive index n_s.

Operating range and detection limit are the other two aspects to evaluate the performance of any sensor. Detection limit corresponds to the minimum variation in the sensed parameter (e.g., % of salinity) which can be detected by a sensor. As far as the operating range is concerned, it is the range of the sensed parameter that a sensor can detect for a given wavelength range. For instance, if one wants to operate the sensor in visible region only, then range of sensed parameter values with their corresponding λ_{res} falling in visible region will decide the operating range of the sensor.

3. RESULTS AND DISCUSSION

Figure 3 shows the variation of transmitted power (P_{trans}) versus wavelength for pure water at four different operating temperatures (T_f) i.e., 25, 50, 75, and 100 °C. The figure is plotted for Ag–Au bimetallic alloy nanoparticle layer with an alloy fraction of 0.4. Thus, Ag nanoparticles consume 40% of the total volume of the alloy nanoparticles. Furthermore, both Ag and Au nanoparticles are assumed to be spherical and of 8 nm size (i.e., $R_{particle}$). The thickness (d) of the whole layer of alloy nanoparticles is taken as 50 nm. The values of other fiber parameters are: numerical aperture (NA) = 0.24, fiber core diameter (D) = 600 μm, and sensing region length (L) = 15 mm.

As can be seen, at different operating temperatures, SPR occurs at different wavelengths for the same sensing medium (i.e., pure water) and keeping the other parameters constant. If these SPR curves are evaluated more closely, two main features become distinctly apparent that with an increase in operating temperature:

(i) The resonance wavelength (λ_{res}) shifts towards the blue. The resonance wavelengths are 541.37 nm, 533.93 nm, 523.75, and 513.05 nm at operating temperatures 25, 50, 75, and 100 °C, respectively.

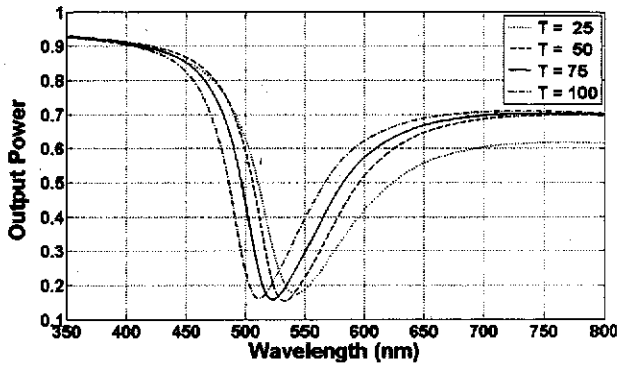

Fig. 3. SPR transmittance curves for fiber optic sensor with Ag–Au bimetallic alloy nanoparticle layer of alloy fraction 0.4 for pure water at four different temperatures (25, 50, 75, and 100 °C).

(ii) The spectral width ($\Delta\lambda_{sw}$) of the SPR curve tends to decrease. The spectral widths are 69.29 nm, 61.39 nm, 57.38 nm, and 53.86 nm at operating temperatures 25, 50, 75, and 100 °C, respectively.

The above two temperature-dependent effects are very important as they influence the sensor's performance in terms of its sensitivity and SNR. Thus, for a clear understanding of this substantial shift in resonance wavelength and sharpening of SPR curve due to variation in operating temperature, more analysis is performed as shown in next section.

3.1. Reasons for Shifting and Sharpening of SPR Curve with Temperature

As discussed earlier, the properties of SPR curves are explained in terms of the matching of resonance condition, i.e., strong transfer of power takes place from incident light to surface plasmons when $K_{ev} = K_{SP}$ at $\lambda = \lambda_{res}$ and the output power encounters a sharp dip.

Figure 4(a) depicts the matching of resonance condition for pure water as well as saline water (with 0.5% salinity) at room temperature (i.e., 25 °C). Figure 4(b) is the corresponding depiction of resonance condition matching at 100 °C operating temperature. Similar to Figure 3, these figures are also plotted for Ag–Au alloy nanoparticles with an alloy fraction (x) of 0.4 and a nanoparticle size of 8 nm. The purpose behind showing these two figures is to observe the effect of temperature-variation on both resonance wavelength shifting as well as on sensitivity. It can be readily observed that for both sensing media, matching of resonance condition occurs at shorter wavelength at higher temperature (i.e., 100 °C). More precisely, the resonance wavelength for pure water shifts from 541.37 nm to 513.05 nm when the operating temperature is raised from 25 °C to 100 °C. This happens via the thermo-optic effect in all the concerned media (i.e., fiber core, alloy nanoparticle layer, and sensing medium) which forces the resonance condition to get satisfied at different wavelengths

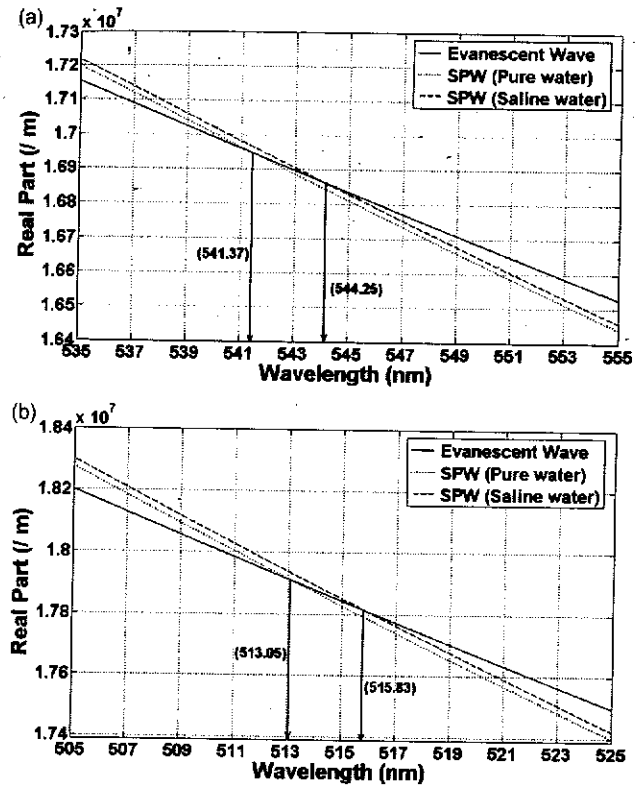

Fig. 4. Variation of real part of surface plasmon propagation constant (K_{SP}) with wavelength corresponding to two sensing media (pure water and saline water) at (a) room temperature, and (b) at 100 °C.

when having different temperatures. Furthermore, the similar effect of blue-shift in resonance wavelength is observed for saline water for which the resonance wavelength shifts from 544.25 nm to 515.83 nm as the operating temperature is varied from 25 °C to 100 °C. However, when these similar effects on the resonance wavelengths of pure and saline water are observed simultaneously, a precise idea about the variation of sensitivity with temperature also becomes clear. At 25 °C, the shift in resonance wavelength for two samples is 2.92 nm (i.e., from 541.37 nm for pure water to 544.25 for saline water with 0.5% salinity). For the same two samples, the shift in resonance wavelength is 2.78 nm (i.e., from 513.05 nm for pure water to 515.83 for saline water) when the operating temperature becomes 100 °C. More precisely, the sensor's sensitivity (S_n) falls to 2.1118 μm/RIU (at 100 °C) from 2.5678 μm/RIU (at 25 °C), which is, indeed, a significant variation. It clearly suggests that any variation in operating temperature not only shifts the resonance wavelength for any sensing medium towards blue but also decreases sensitivity of accurately detecting two samples of slightly different refractive indices. Figure 5 shows the variation of sensitivity with temperature for all six bimetallic alloy combinations. The alloy fraction is 0.4 and particle size is 8 nm for all six combinations. As is visible, sensitivity tends to decrease linearly with an increase in temperature for all the alloy combinations.

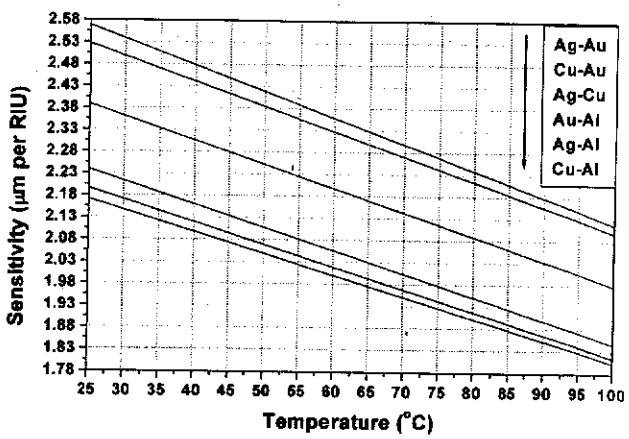

Fig. 5. Variation of sensitivity with temperature for all six bimetallic alloy combinations having alloy fraction of 0.4 and particle size of 8 nm.

Furthermore, it is also important to analyse the effect of temperature variation on another performance parameter, i.e., SNR because shift in resonance wavelength and change in spectral width of SPR curve are bound to alter the SNR of the sensor (see Eq. (17)). Apart from separation of resonance wavelengths for two sensing media, SNR depends on the mean width of the SPR curves corresponding to two sensing media. The spectral width of the SPR curve depends upon the amount of light absorbed by the SPR active region. The imaginary part of the propagation constant of SPW (K_{sp}) corresponds to the absorption caused by the SPR active region and is known as internal damping. In case of large absorption (or internal damping), the SPR curve tends to broaden due to large area covered at wavelength scale. It means that internal damping can give a fair idea about the variation of the spectral width of an SPR curve. Figure 6 shows the variation of internal damping versus wavelength at 25 °C and 100 °C. As above, the curves are plotted for the combination of pure water and Ag–Au alloy with an alloy fraction of 0.4. As can be seen, internal damping has a larger value for a smaller temperature at any wavelength. More precisely, the internal damping decreases with an increase in temperature, therefore, SPR curve width should decrease with an increase in operating temperature. Figure 3 shows the same trend where SPR curve tends to sharpen as the operating temperature is raised to higher values than room temperature. However, there is another explanation, namely radiation damping, which can be added to support this inverse dependence of the SPR curve width with operating temperature. Radiation damping is defined as the proportion of back-scattered light by metal-dielectric interface upon excitation of surface plasmons. This back-scattered light interferes destructively with the incoming light as both are in opposite direction to each other. As the amount of radiation damping increases, SPR curve becomes sharper because radiation damping is able to compensate the incoming light. In the present case, at larger operating temperature, resonance takes place at shorter wavelengths

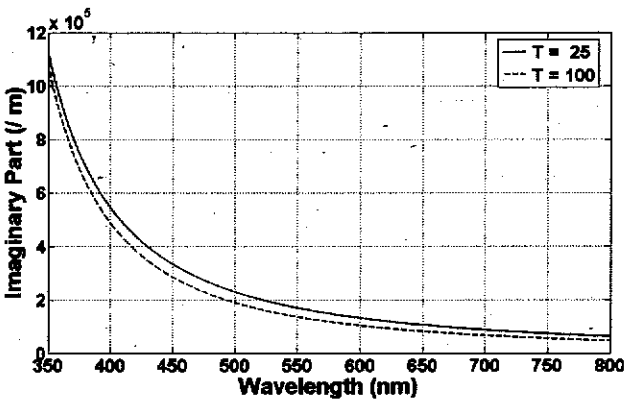

Fig. 6. Variation of imaginary part of surface plasmon propagation constant (K_{SP}) with wavelength corresponding to pure water at 25 °C and 100 °C.

whereas the resonance point shifts to longer wavelengths for smaller temperatures as shown above. Radiation damping is strong if SPR takes place at shorter wavelengths as it has an inverse dependence on excitation wavelength. Therefore, SPR curve is much sharper at larger temperatures due to increased radiation damping, which implies that the SPR curve width is much smaller at larger temperatures. Thus, both internal damping and radiation damping contributes to the sharpening of SPR curve with an increase in temperature.

3.2. Overall Influence of Temperature: Selection of the Suitable Alloy Combinations

As was shown in Figure 5, sensitivity decays linearly with an increase in temperature. The similar trend of sensitivity decay was observed for the whole range of alloy fractions (i.e., between 0 and 1) corresponding to all six bimetallic combinations. Therefore, we calculated the sensitivities corresponding to six alloy combinations for the whole range of alloy fraction at room temperature (Fig. 7(a)). The plots contain the performance of single metal nanoparticle layer at extreme values of alloy fraction, i.e., at $x = 0$ and $x = 1$. For example, in case of Ag–Au alloy, $x = 0$ shows the sensitivity corresponding only to the Au nanoparticle layer, whereas $x = 1$ shows the sensitivity corresponding only to the Ag nanoparticle layer. Then, the temperature gradient of the sensitivity was calculated for whole practical range of bimetallic alloy fractions (0.05 to 0.95) corresponding to all six combinations (Fig. 7(b)). These two figures enable to estimate the decay in sensitivity with temperature for all alloy combinations at their different alloy fractions. Similarly, SNR was also found to increase with temperature in a nearly linear fashion. Therefore, similar kinds of calculations were done for SNR variation at different fractions corresponding to six combinations. Figures 8(a) and (b), respectively, depict the variation of SNR (at room temperature) and temperature-gradient of SNR with alloy fraction for all

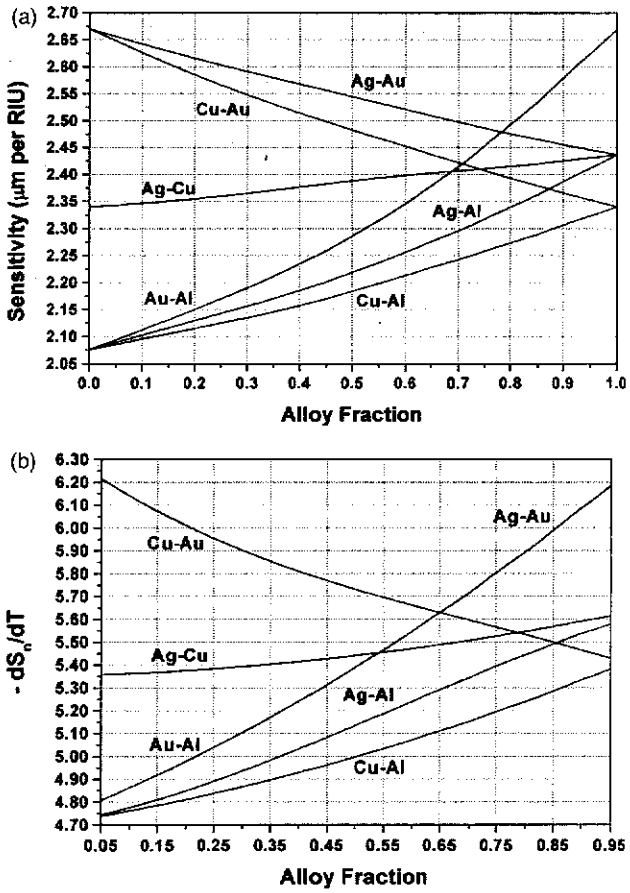

Fig. 7. Variation of (a) sensitivity at room temperature, and (b) temperature-gradient of sensitivity (nm per °C) with alloy fraction for all six bimetallic combinations.

six bimetallic combinations. It is to be noticed that the temperature-gradient of sensitivity is negative because a rise in temperature decreases the sensitivity as explained in the previous section. On the other hand, temperature-gradient of SNR is positive because SNR increases with temperature due to the fact that the decrease in mean SPR curve width has larger magnitude than the difference between resonance wavelengths corresponding to two sensing media.

The next task is to select the bimetallic alloy combinations that are able to provide the best performance against the variation in operating temperature. Before that, it is more appropriate to analyze the performance of alloy combinations at room temperature and find out the combinations that are best performing at room temperature. From Figures 7(a) and 8(a), it is clear that no single alloy combination of metal nanoparticles is able to provide satisfactory values of both SNR and sensitivity, simultaneously. The Cu–Al combination is the most accurate (i.e., having maximum SNR) but the worst sensitive. Au–Al and Ag–Au are the most sensitive but not highly accurate. Since both SNR and sensitivity should be as large as possible, therefore, we are inclined to defy this trade-off and to find a unique value

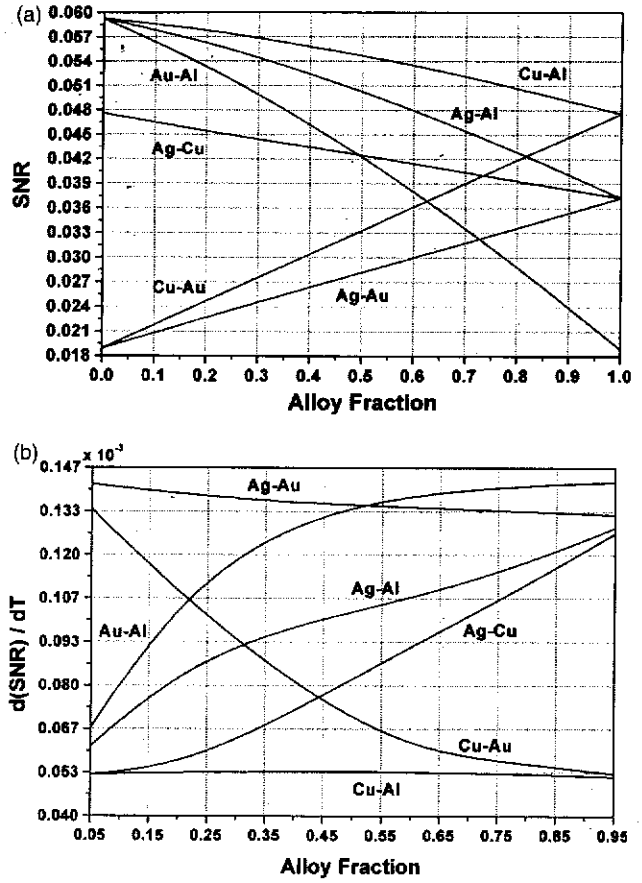

Fig. 8. Variation of (a) SNR at room temperature, and (b) temperature-gradient of SNR (per °C) with alloy fraction for all six bimetallic combinations.

of alloy composition ratio for every bimetallic combination around which one can achieve satisfactory values of both SNR and sensitivity. For that purpose, we define a logical criterion that SNR should not be less than 0.040 and sensitivity should not be less than 2.37 μm per RIU. Both these criterion values of sensitivity and SNR fall approximately in the middle of the respective variation range in Figures 7(a) and 8(a). When we apply this criterion to all the combinations, we find that Ag–Cu in the close vicinity of $x = 0.3$ (SNR = 0.044, $S_n = 2.37$ μm per RIU), Ag–Al at around $x = 0.9$ (SNR = 0.040, $S_n = 2.38$ μm per RIU), and Cu–Au at around $x = 0.8$ (SNR = 0.042, $S_n = 2.39$ μm per RIU) satisfy the above criterion. The other three combinations Ag–Au, Cu–Al and Au–Al do not satisfy the above criterion for any value of alloy fraction. Hence, we can define two categories of bimetallic combinations on the basis of the above criterion. In the first category, Cu–Au with an alloy fraction lying in the vicinity of 0.8 can be classified as the best choice as it provides high values of both SNR and sensitivity, simultaneously. Then comes the Ag–Cu combination at around $x = 0.3$ (due to highest SNR among the three) followed by Ag–Al at around $x = 0.9$. In the second category, Au–Al combination near $x = 0.6$ is able to come almost close to the above criterion with SNR = 0.037 and $S_n = 2.34$ μm per RIU. However, Cu–Al at $x = 0.9$ is able to provide high SNR (0.049) but at the cost of sensitivity, which becomes as small as 2.30 μm per RIU. Further, Ag–Au at $x = 0.9$ shows similar contrast with high sensitivity (2.46 μm per RIU) at the cost of SNR, which is as low as 0.035. Conclusively, it can be stated that the first category (comprising of Cu–Au at around $x = 0.8$, Ag–Cu near $x = 0.3$, and Ag–Al near $x = 0.9$) satisfies the criterion defined above whereas the second category (comprising of Au–Al at $x = 0.6$, Cu–Al at $x = 0.9$ and Ag–Au at $x = 0.9$) does not satisfy the above criterion. Table III provides clear information about the above-mentioned criterion, two categories of bimetallic alloy combinations along with their corresponding sensitivity and SNR values.

Now is the turn to analyze the plots related to temperature-gradients of sensitivity (i.e., Fig. 7(b)) and SNR (i.e., Fig. 8(b)). It can be readily seen that even the temperature-gradients demonstrate a similar trade-off like the accurate sensitivity and SNR values were shown to have at room temperature (i.e., in Figs. 7(a) and 8(a)). This is the reason why we constricted the range of alloy fractions between 0.05 and 0.95 in Figures 7(b) and 8(b) in order to make the analysis a little easier. The most obvious trade-off is that sensitivity decays whereas SNR improves with an increase in temperature. Further, if any alloy combination shows smaller temperature-gradient for sensitivity, the corresponding gradient for SNR is also small. All in all, it is clearly not possible to choose any alloy combination and its specific alloy fraction which are best-placed to perform better than other combinations against temperature variation. The prime objective here is that the decay in sensitivity should be compensated by an increase in SNR. Therefore, we again try to apply a criterion to make a logical selection. We assume that the temperature-gradient for sensitivity should not be larger than 5.50 nm RIU^{-1} per °C and for SNR it should not be smaller than 0.097×10^{-3} per °C. As was seen previously for different alloy ratios, both these values fall almost in the middle of the whole corresponding ranges of temperature-gradients. When we apply the criterion, we find that Ag–Au and Cu–Al never satisfy this criterion, i.e., Ag–Au always satisfies the criterion's SNR-related part but never fulfils the sensitivity-related part and exactly the inverse is true for Cu–Al. Furthermore,

Table III. Comparison criterion, alloy categories, and performance parameters at $T = 25$ °C.

Category	Alloy combination (approx. alloy fraction)	S_n (μm/RIU)	SNR
I Criterion:	Cu–Au (0.8)	2.39	0.042
$S_n \geq 2.37$ μm/RIU	Ag–Cu (0.3)	2.37	0.044
and SNR ≥ 0.040	Ag–Al (0.9)	2.38	0.040
II Criterion:	Au–Al (0.6)	2.34	0.037
$S_n < 2.37$ μm/RIU	Cu–Al (0.9)	2.30	0.049
and SNR < 0.040	Ag–Au (0.9)	2.46	0.035

Cu–Au satisfies the SNR-part for x values lying between 0.05 and 0.25, but the sensitivity part for x lying between 0.85 and 0.95. Therefore, there is no common x-value at which both parts are satisfied simultaneously. However, it can be found that Au–Al (for $0.17 < x < 0.57$), Ag–Al (for $0.40 < x < 0.85$), and Ag–Cu (for $0.66 < x < 0.68$) are able to satisfy the whole criterion. Therefore, we can make two categories: One consisting of Ag–Au, Cu–Al, and Cu–Au that are not able to simultaneously satisfy the criterion related to temperature-gradient, and second one consisting of Ag–Al, Au–Al, and Ag–Cu which are able to satisfy the above criterion corresponding to their particular ranges of x-values.

When we combine the categories for SNR and sensitivity at room temperature with those for corresponding temperature-gradients, it is found that the optimized x-value (i.e., around 0.9) of Ag–Al at room temperature is in the close vicinity of the optimized x-range in context of temperature variation (i.e., 0.40–0.85). So, Ag–Al may be the best choice as it provides better overall performance than the other combinations at any temperature. The Au–Al combination can be put as a second choice in the context of temperature variation for two reasons. First, it's optimized x-value at room temperature (i.e., around 0.6) nearly satisfies the criterion set at room temperature for SNR and sensitivity. Second, the above x-value falls very close to its corresponding optimized x-range against temperature variation (i.e., 0.17–0.57). The Ag–Cu combination has two drawbacks. First, it has a very narrow range of x-values (0.66–0.68) optimized against temperature variation. Second, its corresponding optimized x-value at room temperature (i.e., around 0.3) is far from the above values (0.66–0.68).

3.3. Salinity Sensor

After optimizing the bimetallic nanoparticle alloy fraction with respect to the temperature variation for simultaneously obtaining satisfactory sensitivity and SNR values, the final task is to obtain the calibration for the salinity sensor along with the other two performance parameters, i.e., operating range and detection limit. Figure 9(a) depicts the calibration graphs of resonance wavelength versus salinity at four different temperatures for Ag–Al alloy combination having an alloy fraction of 0.85. It is readily visible in Figure 9(a) that at all temperatures, the resonance wavelength continuously shifts to a higher value as the salinity percentage increases in the water sample. Furthermore, at a given value of salinity percentage in the water sample, the resonance wavelength shifts towards blue with an increase in operating temperature. For the whole range of salinity (i.e., from 0 to 20%), the resonance wavelengths are found to be comfortably falling inside the visible spectral region at any given temperature. Figure 9(b) shows the corresponding calibration curves for Au–Al alloy combination having

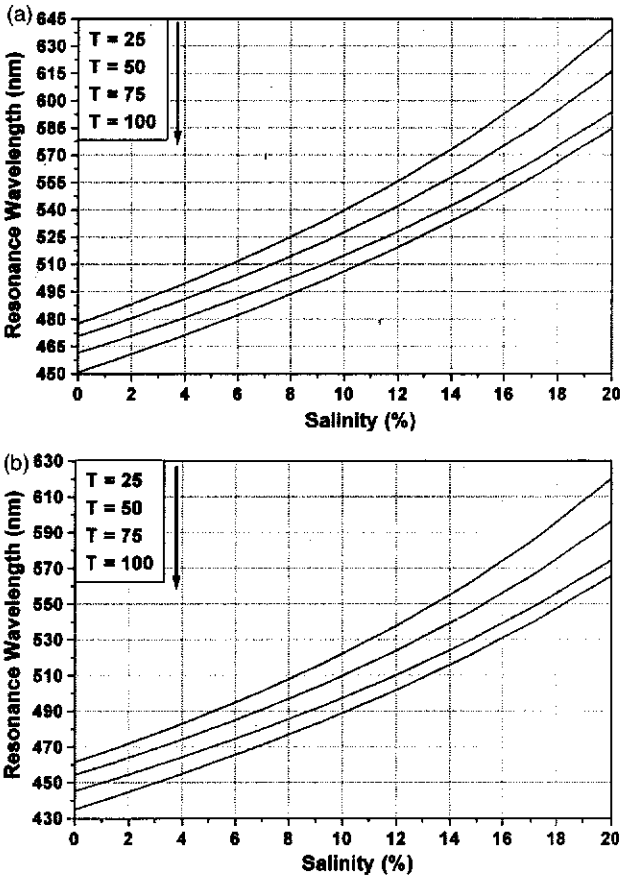

Fig. 9. Calibration curves (% salinity vs. resonance wavelength) for (a) Ag–Al (with 0.85 alloy fraction), and (b) Au–Al (with 0.57 alloy fraction) at four different temperatures (25, 50, 75, and 100 °C).

an alloy fraction of 0.57. All the above-mentioned observations are true for Au–Al alloy combination as well.

Regarding the theoretical detection limit of the sensor, with the normally available detectors having a spectral resolution of 0.01 nm, both above alloy fractions with their respective optimized alloy fractions are able to provide a variation of the order of as small as 10^{-3}% salinity in the water sample at any operating temperature. It means that both above alloy combinations may detect the salinity of the order of as small as 0.01 g in 1 Kg of water sample. However, there is a slight decrease in detection limit with an increase in operating temperature. More precisely, the overall detection limit for both the optimized alloy combinations vary approximately from 1.2×10^{-3}% (for $T = 25$ °C) to 1.5×10^{-3}% (for $T = 100$ °C) of salinity in the water sample. Notably, the order (10^{-3}% salinity) of detection limit remains in tact even when the temperature varies from 25 °C to 100 °C.

Regarding the operating range, at any operating temperature, the present fiber optic SPR salinity sensor with any of the optimized alloy combinations exhibits a wide operating range with respect to salinity percentage. This is because resonance wavelengths for such a wide salinity range are within the visible spectral region only. Moreover,

both alloy combinations still have sufficient scope to detect more salinity present in the water sample. Interestingly, the smaller the operating temperature the wider is the operating range with respect to salinity percentage for both the alloy combinations.

Thus, the above two alloy combinations (Ag–Al and Au–Al) with their optimized alloy fractions (i.e., 0.85 and 0.57, respectively) are able to provide an overall high sensing performance concerning salinity detection in the water sample because both of them do not only have high values of sensitivity and SNR (as optimized in the previous section) but also exhibit wide operating ranges and sharp detection limits at any temperature.

4. CONCLUSIONS

In conclusion, a new theoretical model for fiber optic SPR salinity sensor based on bimetallic alloy nanoparticle layer is proposed. Based on rigorous numerical calculations, it was found that that no single metal nanoparticle coating (i.e., Ag, Au, Al, and Cu) is able to provide reasonable values for both main performance parameters i.e., sensitivity and SNR, simultaneously. Nevertheless, when the nanoparticles of these metals are used in bimetallic combinations of well-defined alloy fractions, one can find a balanced overall sensing performance with high sensitivity and SNR. The proposed bimetallic alloy combinations were classified in two categories based on a logical criterion. In the first category, three alloy combinations Cu–Au, Ag–Cu, and Ag–Al with their alloy fractions in the vicinity of 0.8, 0.3, and 0.9, respectively, are able to show significantly high values of sensitivity and SNR, simultaneously. The sensor's performance is further optimized against the variation in operating temperature. It was found that Ag–Al and Au–Al alloy combinations with well-defined alloy fractions are found to show much balanced performance in terms of SNR and sensitivity compared to the other alloy combinations. Furthermore, the calibration curves, operating range, and detection limit for the proposed salinity sensor were in full accordance with the optimization of sensitivity and SNR against thermal variation.

In summary, a new theoretical model for the SPR sensing of salinity in any water sample has been presented. The proposed model can be considered as a sufficient starting point for a further research and development on fiber optic salinity sensor based on SPR. Such a salinity sensor has a lot of advantage in liquid systems such as in environmental and physio-chemical systems where *in situ* detection of salinity becomes a very crucial factor.

Acknowledgment: Anuj Kumar Sharma is grateful to the Alexander von Humboldt Foundation (Germany) for financial support during his research stay at Friedrich-Schiller University of Jena.

References and Notes

1. B. Liedberg, C. Nylander, and I. Sundström, *Sens. Actuators* 4, 299 (**1983**).
2. F. Villuendas and J. Pelayo, *Sens. Actuators, A, Phys.* 23, 1142 (**1990**).
3. R. C. Jorgenson and S. S. Yee, *Sens. Actuators, B, Chem.* 12, 213 (**1993**).
4. J. Homola, *Sens. Actuators, B, Chem.* 41, 207 (**1997**).
5. E. Kretschmann, *Z. Phys.* 241, 313 (**1971**).
6. S. F. Cheng and L. K. Chau, *Anal. Chem.* 75, 16 (**2003**).
7. A. K. Sharma and B. D. Gupta, *Nanotechnology* 17, 124 (**2006**).
8. Z. Qi, I. Honma, and H. Zhou, *Opt. Letters* 31, 1854 (**2006**).
9. A. K. Sharma and G. J. Mohr, *J. Physics D: Applied Physics* 41, 055106 (**2008**).
10. G. Ghosh, M. Endo, and T. Iwasaki, *J. Lightwave. Tech.* 12, 1338 (**1994**).
11. U. Kreibig, *J. Phys. F: met. Phys.* 4, 999 (**1974**).
12. H. P. Chiang, P. T. Leung, and W. S. Tse, *J. Chem. Phys.* 108, 2659 (**1998**).
13. S. K. Ozdemir and G. T. Sayan, *J. Lightwave. Technol.* 21, 805 (**2003**).
14. T. Holstein, *Phys. Rev.* 96, 535 (**1954**).
15. J. A. McKay and J. A. Rayne, *Phys. Rev. B* 13, 673 (**1976**).
16. R. T. Beach and R. W. Christy, *Phys. Rev. B* 16, 5277 (**1977**).
17. W. E. Lawrence, *Phys. Rev. B* 13, 5316 (**1976**).
18. P. Debye, *Ann. Physik* 39, 789 (**1912**).
19. P. Scheibener, J. Straub, J. M. H. Levelt Sengers, and J. S. Gallagher, *J. Phys. Chem. Ref. Data* 19, 677 (**1990**).
20. S. C. McCutcheon, J. L. Martin, and T. O. Barnwell, Handbook of Hydrology, 2nd edn., McGraw-Hill, New York (**1993**), Vol. 1.

Received: 14 March 2009. Accepted: 8 August 2009.